

# Design and preparation of shape memory phenol–formaldehyde foam composites with excellent thermal stability and mechanical properties

Likai Hu<sup>a</sup>, Fenghua Zhang<sup>a</sup>, Lan Luo<sup>a</sup>, Linlin Wang<sup>a</sup>, Yanju Liu<sup>b</sup>, Jinsong Leng<sup>a,\*</sup>

<sup>a</sup> Centre for Composite Materials and Structures, Harbin Institute of Technology (HIT), No. 2 Yikuang Street, Harbin 150000, People's Republic of China

<sup>b</sup> Department of Astronautic Science and Mechanics, Harbin Institute of Technology (HIT), No. 92 West Dazhi Street, Harbin 150000, People's Republic of China

## ARTICLE INFO

### Keywords:

A. Smart materials  
A. Foams  
B. Mechanical properties  
E. Foaming

## ABSTRACT

Phenolic resins equipped with flame retardant and exceptional ablative properties show considerable potential for thermal protection applications. However, phenolic resins typically exhibit poor mechanical properties, as they are brittle, easily pulverized, and difficult to deform. In this study, shape memory phenol–formaldehyde resins (SMPRs) were synthesized through chemical cross-linking reactions and prepared shape memory phenol–formaldehyde foams (SMPFs) using physical foaming techniques. SMPFs exhibited good shape memory properties and deformation capabilities. Compared with other shape memory polymer foams, the SMPFs presented superior thermal stability, and a superior residual carbon rate. Shape memory polymer foam composites (SMPFCs) reinforced with SiO<sub>2</sub> or Al<sub>2</sub>O<sub>3</sub> nanoparticles demonstrated improved thermal stability, and were capable of completing a self-expanding and self-folding process. SMPFs and SMPFCs have the potential to be applied in flexible fireproof materials owing to their excellent deformation properties and high-temperature resistance.

## 1. Introduction

A type of smart material, shape memory polymers (SMPs) are capable of perceiving changes to their external environment and conducting shape transitions actively [1–4]. Shape memory polymer foam, a new class of smart polymer material that has a porous structure based on SMPs and integrates the merits of ordinary foams and SMPs, presents the character of lightweight, high compression rate, and good shape memory effect [5–10]. In addition, shape memory polymer foams exhibit a higher shape recovery rate and a shorter response time than SMPs [11]. Therefore, shape memory polymer foams demonstrate potential for application in various fields [12–15]. In 2004, Composite Optics Inc. (COI) and Jet Propulsion Laboratory (JPL) introduced a foam truss structure. The Cornerstone Research Group (CRG) also suggested the use of shape memory polymer foam as a honeycomb material in self-deforming *trans*-dimensional unmanned aerial vehicle (UAV) wings to maintain wing shape during deformation. Santo et al. [16] envisaged the potential application of shape memory polymer foam in solar sails, proposing that enhancing the stiffness of the shape memory polymer foam with carbon nanotubes, compressing, packaging, and subsequently launching it into space, where it could be propelled through the shape

recovery of the shape memory polymer foam actuated by solar energy. Santo et al. [17] performed bending, compression, and torsion experiments on shape-memory epoxy foams in space, confirming that shape memory epoxy foam retained its shape memory characteristics in the harsh space environment, which provided a crucial theoretical foundation for the application of shape memory polymer foams in the aerospace sector. Leng et al. [18] utilized shape memory polymer foam in a flexible solar-array system (SMPF-FSAS) and accomplished the first spaceflight demonstration of an SMPF-FSAS in orbit, justifying the utility of SMPF in oversized space deployable structures.

The small number of varieties and poor thermal stability of the currently reported shape memory polymer foams limit their application scope. With the development of industrial technology, there is an increasing need for high-performance foam materials, prompting an increasing number of researchers to enhance and modify phenolic foam to mitigate its limitations [19–21]. In recent decades, several strategies for toughening phenolic-formaldehyde foams have been explored, and these strategies can be divided into two broad categories: physical blending and chemical modification [22–27]. Yu et al. [28] assessed the impact of particles on foam properties and microstructure by producing two phenolic foams modified with both expandable and expanded

\* Corresponding author.

E-mail address: [lengjs@hit.edu.cn](mailto:lengjs@hit.edu.cn) (J. Leng).

<https://doi.org/10.1016/j.compositesa.2023.107738>

Received 15 May 2023; Received in revised form 28 July 2023; Accepted 10 August 2023

Available online 10 August 2023

1359-835X/© 2023 Elsevier Ltd. All rights reserved.

graphite. They discovered that both expandable and expanded graphite increased the compressive modulus of the foams considerably. Sui et al. [29] modified the phenolic resin with a polyethylene glycol phosphate toughening agent and fabricated lightweight phenolic foams of different compositions. They found that foam composites had a more uniform microscopic pore structure than phenolic foams, as revealed via scanning electron microscopy. The introduction of phosphorus elements also enhanced the fire-resistant properties of phenolic foams. Luo et al. [30] prepared phenolic composite foams by embedding graphene oxide (GO)/SiO<sub>2</sub> hybrids of varying sizes into phenolic resins. Deng et al. [31] investigated deformable phenolic resins by integrating flexible chain segments of polyurethane prepolymers into phenolic structures. However, the polyurethane prepolymer substantially reduced the thermal stability of the phenolic resin, which limited the application scope. Hence, the development of shape memory phenolic foam with good deformability as well as high thermal stability is urgently required.

In this study, a shape memory phenol-formaldehyde resin (SMPR) with aliphatic chain work as soft segment and aromatic structure work as hard segments was synthesized, and the corresponding shape memory phenol-formaldehyde foam (SMPF) was prepared via physical foaming.

The shape memory polymer foam composites (SMPFCs) were fabricated by incorporating inorganic nanoparticles to further enhance the thermal stability and mechanical properties of the foam. The mechanical properties, deformability, thermal stability and shape memory properties of the SMPRs, SMPFs and SMPFCs were investigated thoroughly. It was shown that the foam can be deformed into a temporary shape by force after being heated above the glass transition temperature (T<sub>g</sub>). After cooling below T<sub>g</sub> and removing the applied force, the obtained temporary shape could be frozen. Notably, the foam can recover to its original shape upon reheating the temperature above T<sub>g</sub>, as shown in Fig. 1(c). SMPFC with excellent mechanical properties is expected to be used as a load support structure in building construction. The outstanding expansion capabilities offer the possibility of SMPFC acting as a blocking agent. With its superior deformability and thermal stability properties, SMPF has potential applications in aerospace flexible devices and flexible fireproof materials.

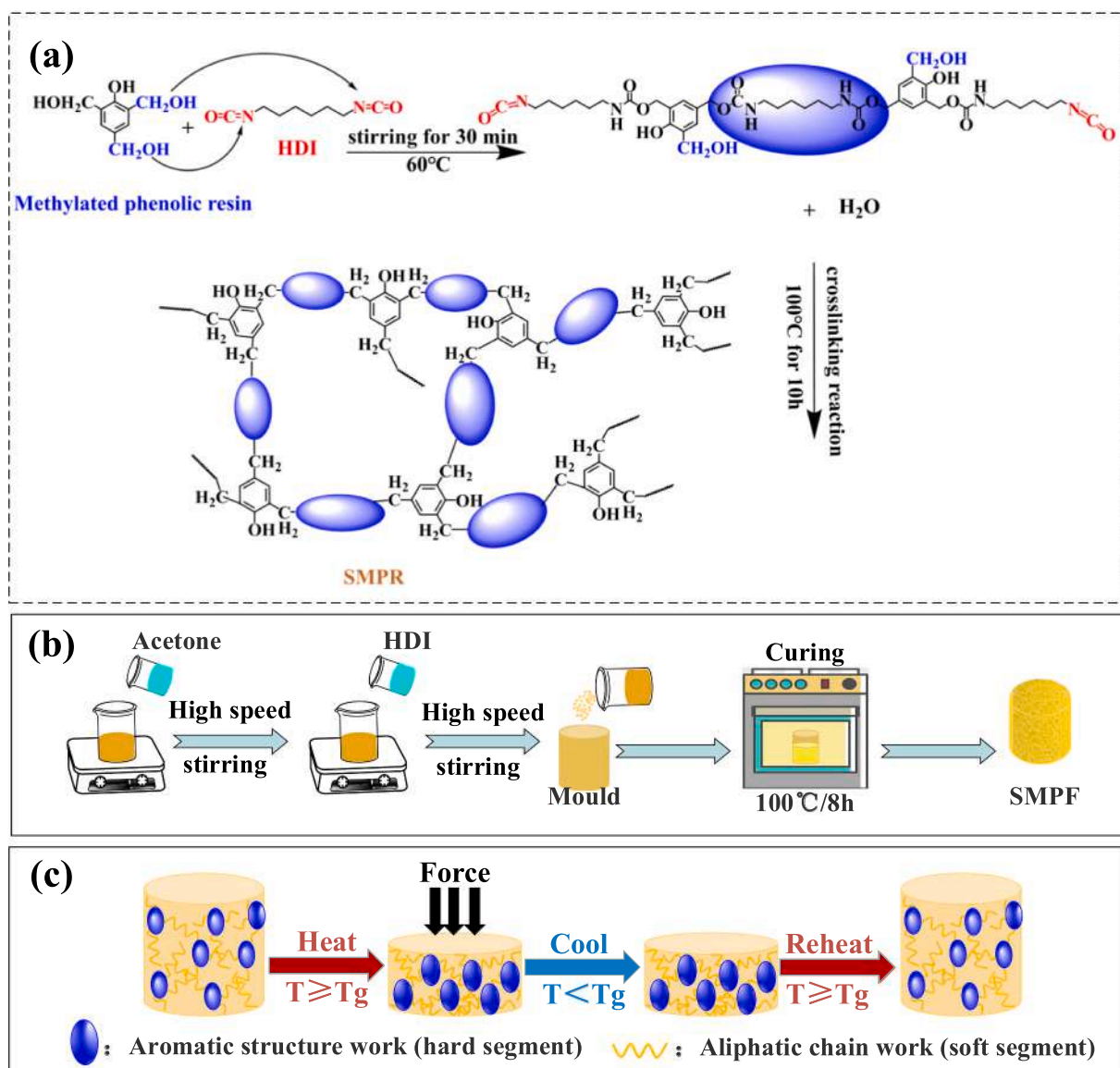


Fig. 1. (a) Schematic of the synthesis process of SMPR; (b) schematic diagram of the preparation process of SMPF; (c) schematic diagram of shape memory mechanism of SMPF.

## 2. Experimental section

### 2.1. Materials

Methyl phenolic solution (90 %) with a molecular weight of 200 was supplied by Hebei Zetian Chemical Co., China. Hexamethylene diisocyanate (HDI), p-toluenesulfonic acid, Twain 85, n-Pentane, and acetone were purchased from Aladdin Reagent (Shanghai) Co, China.

### 2.2. Synthesis of shape memory phenol-formaldehyde

Firstly, 50 g of methyl phenolic solution was added to a 250-mL beaker and treated under vacuum for 20 min at 60 °C to remove the ethanol from the solution and obtain methyl phenolic resin. Following that, 20 g of methylated phenolic resin was dissolved in 20 g of acetone and transferred to a beaker. Subsequently, according to the mass ratio (Table 1), HDI and p-toluenesulfonic acid were added to the beaker for a 5 h reaction at 60 °C. Then, the temperature was raised to 100 °C and maintained for 10 h to obtain brownish-red transparent SMPR. The SMPRs obtained with different ratios were denoted SMPR-1, SMPR-2, SMPR-3, and SMPR-4. The chemical equations involved are shown in Fig. 1(a).

### 2.3. Preparation of shape memory phenolic-formaldehyde foam

Firstly, methyl phenolic resin and HDI were added into a beaker via constant stirring according to the mass ratios listed in Table 2. Then, 2 g of p-toluenesulfonic acid and 2 g of n-Pentane were added into the beaker via rapid stirring to ensure thorough mixing. The mixture was poured into the mould and cured at 100 °C for 8 h. Afterwards, the SMPFs were obtained by cooling to room temperature and demoulding. [32] The SMPFs obtained with different ratios were denoted SMPF-1, SMPF-2, SMPF-3, and SMPF-4. The formulation process of the foam is illustrated in Fig. 1(b).

### 2.4. Preparation of shape memory phenolic-formaldehyde composite foam

Firstly, according to the mass ratio (Table 3), methyl phenolic resin and the fumed silica powder were put into the beaker, stirred continuously and then mixed via ultrasonic shaking. Physical foaming was then carried out according to the method in Section 2.3 to obtain the fumed silica-reinforced shape memory phenolic-formaldehyde foams. The foams obtained with different ratios were denoted SMPF/SiO<sub>2</sub>-1, SMPF/SiO<sub>2</sub>-2, SMPF/SiO<sub>2</sub>-3 and SMPF/SiO<sub>2</sub>-4 respectively. Shape memory phenolic-formaldehyde composite foams reinforced with alumina powder were prepared similarly. The foams obtained with different ratios denoted SMPF/Al<sub>2</sub>O<sub>3</sub>-1, SMPF/Al<sub>2</sub>O<sub>3</sub>-2, SMPF/Al<sub>2</sub>O<sub>3</sub>-3 and SMPF/Al<sub>2</sub>O<sub>3</sub>-4 respectively (see Table 4).

### 2.5. Characterization

Fourier-transform infrared spectroscopy (FTIR, Nicolet iS10, Nicolet Instrument Crop) was used to determine the chemical bonding of SMPRs in a wavelength range of approximately 4000–500 cm<sup>-1</sup> at a resolution of 4 cm<sup>-1</sup>.

A dynamic thermodynamic analyser (DMA, NETZSCH Q800, TA, US) was used to determine the dynamic mechanical properties of these samples. The samples were 40 × 3 × 1 mm in size. The experiments were

**Table 1**  
SMPRs with different formulations.

Samples	SMPR-1	SMPR-2	SMPR-3	SMPR-4
Methylated phenolic resin (g)	20	20	20	20
HDI (g)	2	3	4	5

**Table 2**  
SMPFs with different formulations.

Samples	SMPF-1	SMPF-2	SMPF-3	SMPF-4
Methylated phenolic resin (g)	20	20	20	20
HDI (g)	2	3	4	5
p-toluenesulfonic acid (g)	2	2	2	2
n-Pentane (g)	2	2	2	2

**Table 3**  
SMPF/SiO<sub>2</sub>s with different formulations.

Samples	SMPF/ SiO <sub>2</sub> -1	SMPF/ SiO <sub>2</sub> -2	SMPF/ SiO <sub>2</sub> -3	SMPF/ SiO <sub>2</sub> -4
Methylated phenolic resin (g)	20	20	20	20
HDI (g)	5	5	5	5
p-toluenesulfonic acid (g)	2	2	2	2
n-Pentane (g)	2	2	2	2
Fumed silica powder (g)	1	1.5	2	2.5

**Table 4**  
SMPF/Al<sub>2</sub>O<sub>3</sub>s with different formulations.

Samples	SMPF/ Al <sub>2</sub> O <sub>3</sub> -1	SMPF/ Al <sub>2</sub> O <sub>3</sub> -2	SMPF/ Al <sub>2</sub> O <sub>3</sub> -3	SMPF/ Al <sub>2</sub> O <sub>3</sub> -4
Methylated phenolic resin (g)	20	20	20	20
HDI (g)	5	5	5	5
p-toluenesulfonic acid (g)	2	2	2	2
n-Pentane (g)	2	2	2	2
Alumina powder (g)	1	1.5	2	2.5

carried out at 3 °C.min<sup>-1</sup> in a range of 25–150 °C.

Thermogravimetric analyses of SMPRs, SMPFs, and SMPFCs were performed using a thermogravimetric analyser (TGA/DSC1, Mettler-Toledo, Switzerland). The experiments were carried out at 3 °C.min<sup>-1</sup> between temperature and 1000 °C under a flowing-nitrogen atmosphere. The thermal stability of the material under air was tested at 3 °C.min<sup>-1</sup> under a flowing air environment between room temperature and 800 °C.

The compression properties of the SMPFs were studied at room temperature and high temperature using a CMT6104 universal testing machine. The compression samples were cylindrical, and each had a diameter and height of 10 mm.

The microstructures of the SMPFs and SMPFCs were studied by a scanning electron microscope (SEM). To obtain a test sample, the foam was cut with a smooth blade to obtain a clean fracture section.

Shape memory performance is one of the most important properties of SMPFs and is strongly related to the temperature range over which SMPFs are used in engineering. The shape memory behaviour of the SMPFs was characterized by the shape recovery rate, shape fixity rate, and thermomechanical cycle tests [33]. The shape memory cycle of SMPFs is shown in Fig. 1(c). The shape fixity rate ( $R_f$ ) and shape recovery rate ( $R_r$ ) of the SMPFs were measured using the following equation:

$$R_f = \frac{h_0 - h_2}{h_0 - h_1} \quad (1)$$

where  $h_0$  is the initial height of the SMPFs,  $h_1$  is height of the SMPFs after cooling and unloading, and  $h_2$  is the height of the SMPFs after an interval.

The shape recovery rate of the SMPFs is calculated by the following equation.

$$R_r = \frac{h}{h_0} \quad (2)$$

where  $h$  is the initial height of the SMPFs and the  $h_0$  is the height of the SMPFs after heating recovery.

### 3. Result and discussion

#### 3.1. Chemical structure of shape memory phenolic resins

In this study, the characteristic chemical groups of the materials were confirmed by FTIR to establish the extent of the reaction. In the FTIR curve for SMPRs (Fig. 2(a)), the infrared absorption peak for the phenolic hydroxyl group was observed at approximately  $3419 \text{ cm}^{-1}$ . The characteristic peak for the aldehyde group appeared at  $2915 \text{ cm}^{-1}$ , and the weak absorption peak at  $1380 \text{ cm}^{-1}$  is the bending vibration peak of isocyanate in the infrared spectra of SMPR-1, SMPR-2, SMPR-3, and SMPR-4, originating from the mixed absorption peak of the carbamate group ( $-\text{HNCOO}-$ ) and the hydrogen-bonded carbonyl group. However, this bending vibration peak did not appear in the IR spectrum of phenolic resin (PR). Moreover, the stretching vibration peak for the isocyanate group ( $\text{N}=\text{C}=\text{O}$ ) near  $2275\text{--}2250 \text{ cm}^{-1}$  was absent in the spectra of the SMPRs. The characteristic peak of the carbonyl group in carbamate emerged at  $1615 \text{ cm}^{-1}$ . When compared with SMPRs, the absorption peak at  $1380 \text{ cm}^{-1}$  was not observed in the spectrum of PR, because PR lacks the isocyanate group found in the soft segment. The FTIR spectra of the four SMPFs is shown in Fig. 2(b). Compared with SMPRs, the characteristic peaks of phenolic hydroxyl group ( $\text{Ar}-\text{OH}$ ) were slightly displaced by the small molecules contained in the foam, however, the positions of all characteristic peaks remained the same essentially. Fig. 2(c) and Fig. 2(d) depict the FTIR spectra of SMPFC. In

the FTIR curve of SMPF/ $\text{Al}_2\text{O}_3$ , the composite exhibits the characteristic peak of alumina at  $465 \text{ cm}^{-1}$  in addition to all chemically characteristic peaks of SMPF. A similar phenomenon was found in the spectra for SMPF/ $\text{SiO}_2$ , where the characteristic peak of the silicon oxide group was found at  $470 \text{ cm}^{-1}$ .

#### 3.2. Thermal properties of shape memory phenolic foams and shape memory phenolic foam composites

TGA curves of SMPF obtained under air and nitrogen conditions were used to evaluate the thermal stability performance of the material and to determine the maximum service temperature ensure safe working conditions. As shown in Fig. 3(a), the decomposition endpoint temperature for SMPFs in air was approximately  $650 \text{ }^\circ\text{C}$ . When the temperature increased to  $1000 \text{ }^\circ\text{C}$ , the remaining weight fractions for SMPF-1, SMPF-2, SMPF-3, and SMPF-4 were 6.86 %, 6.53 %, 6.32 %, and 6.03 %, respectively. An incremental decrease in the residual mass fraction of the foam was observed with an increase in the proportion of soft chain segments.

Fig. 3(b) shows the derivative thermogravimetric (DTG) curve, which is calculated from the first-order differentiation of the TGA curve, and provides a more direct representation of the thermal weight loss rate. Combining information from Fig. 3 (a) and Fig. 3 (b) demonstrate that the thermal decomposition of SMPF under air can be divided into four stages. In the first stage, the principal mass loss originated from free water in the SMPF and the volatilisation of the solvent, and occurred between  $70$  and  $120 \text{ }^\circ\text{C}$ . The weight loss at this stage was less than 2 %. In the second stage, the aldehyde group in the phenolic molecule and the methylene group in the side chain decomposed within between  $120$  and  $300 \text{ }^\circ\text{C}$ , resulting in a 15–20 % weight loss. In the third stage, spanning  $300\text{--}410 \text{ }^\circ\text{C}$ , the carbamate group broke down into isocyanates and

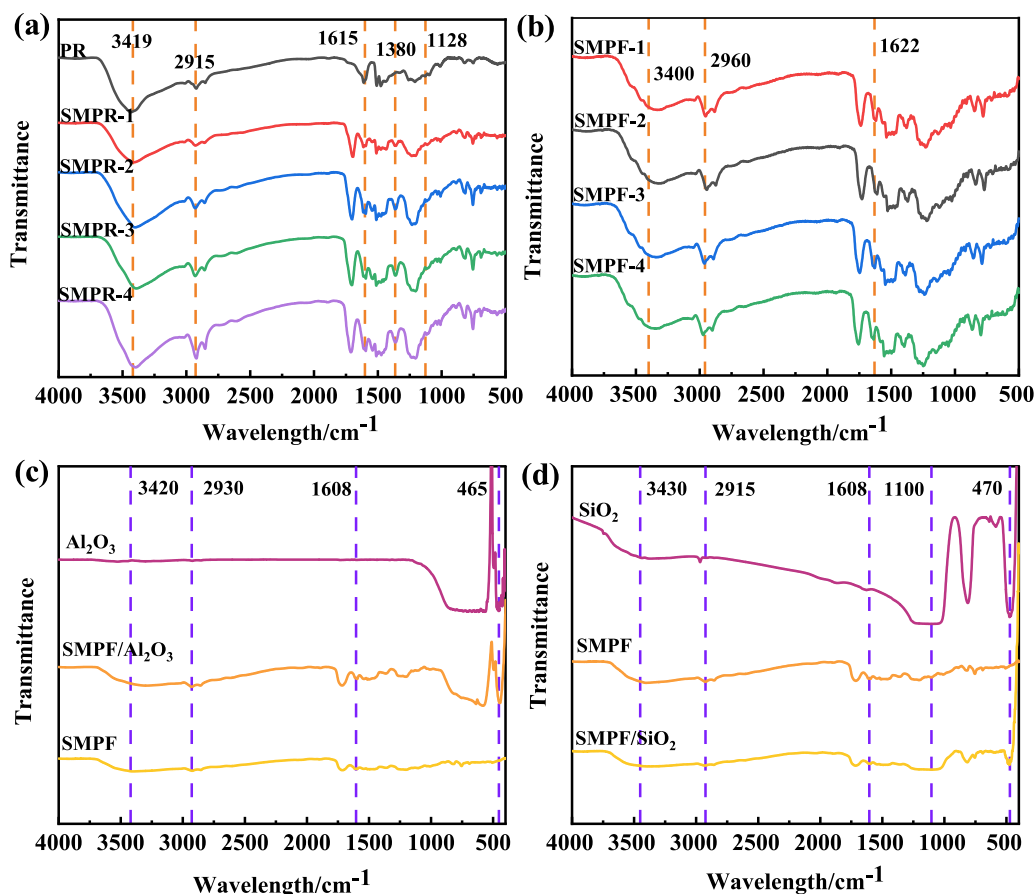


Fig. 2. FTIR spectra in the wavenumber range of  $4000\text{--}500 \text{ cm}^{-1}$  of (a) SMPRs, (b) SMPFs, (c) SMPF/ $\text{Al}_2\text{O}_3$ , and (d) SMPF/ $\text{SiO}_2$ .

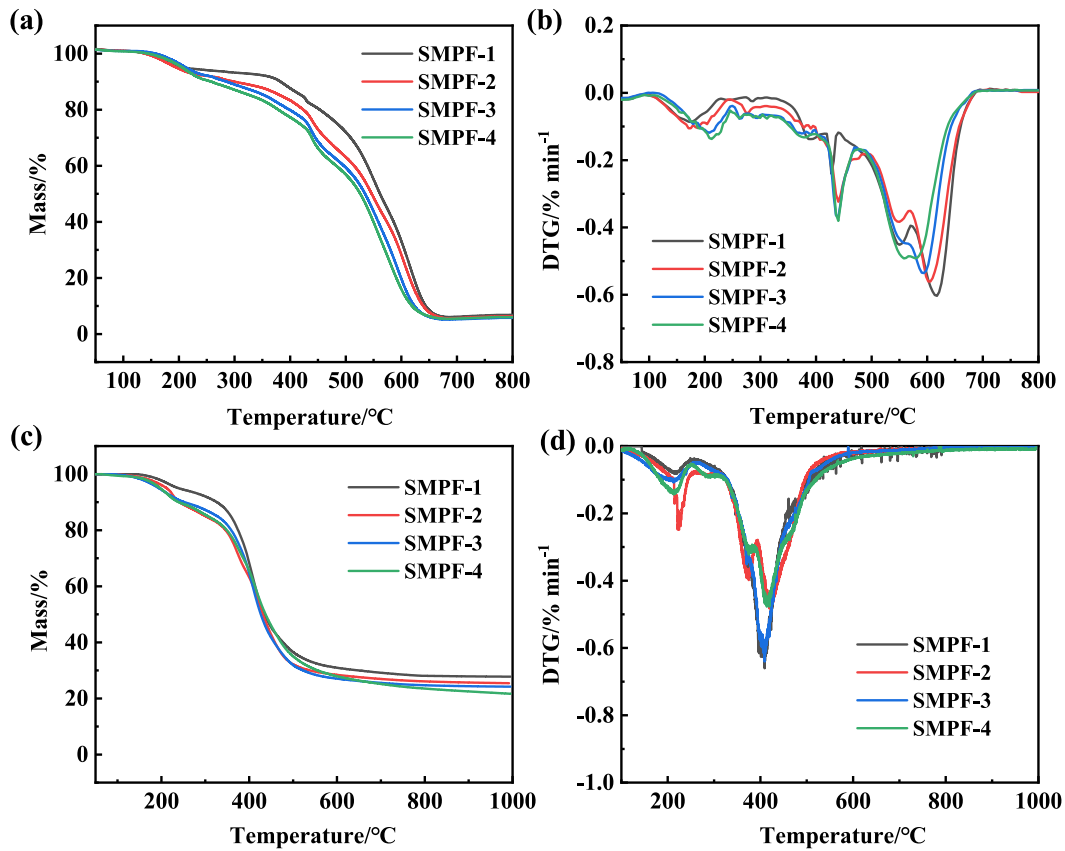


Fig. 3. (a) TGA curve of SMPFs under air; (b) DTG curve of SMPFs under air; (c) TGA curve of SMPFs under nitrogen; (d) DTG curve of SMPFs under nitrogen.

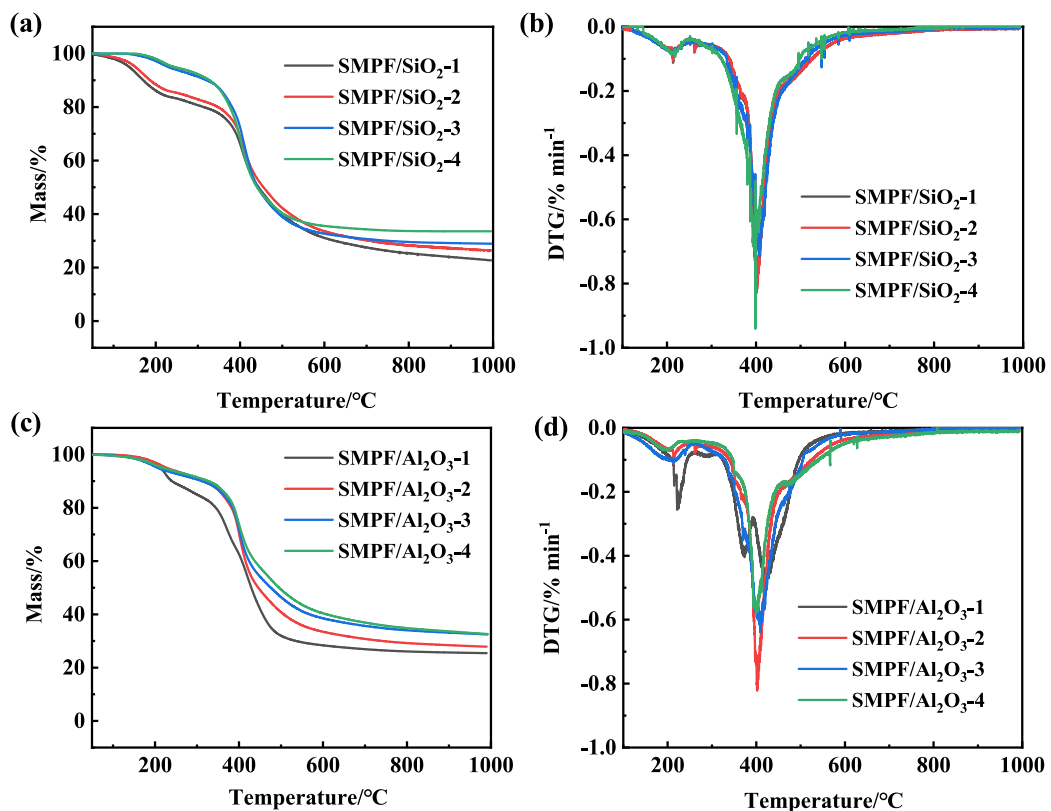


Fig. 4. (a) TGA curve of SMPF/SiO<sub>2</sub>s; (b) DTG curve of SMPF/SiO<sub>2</sub>s; (c) TGA curve of SMPF/Al<sub>2</sub>O<sub>3</sub>s; (d) DTG curve of SMPF/Al<sub>2</sub>O<sub>3</sub>s.

polyols, and further decomposed into amines, alkenes, and  $\text{CO}_2$ , with concurrent fragmentation of several methylene groups. In the final stage, the SMPR backbone and phenolic hydroxyl groups underwent thermal decomposition at 410–800 °C, dehydrating and cyclising into carbon. TGA tests revealed that the quantity of HDI utilised during the reaction process impacted the thermogravimetric properties of SMPFs. The final residual mass ratio of SMPF at 800 °C diminished with increasing HDI usage because the HDI component was completely pyrolyzed at 800 °C, leaving the phenolic pyrolysis in the form of carbon.

To ascertain the service temperature of the foam under nitrogen, TGA tests were conducted. The TGA and DTG curves showed different results compared to those obtained in air (Fig. 3(c) and (d)). As the temperature increased to 1000 °C, the residual mass fraction of SMPF declined, however, it remained higher than when tested under air at all times. The ultimate weight fractions for SMPF-1, SMPF-2, SMPF-3, SMPF-4 were 27.86 %, 25.53 %, 24.32 %, and 23.03 %, respectively. The thermal decomposition of SMPF under air can be divided into three stages. The first stage saw the most rapid SMPF mass loss at 200 °C due to the volatilisation of small molecules such as blowing agents and surfactants, resulting in an 8–15 % reduction in SMPF weight. The second stage, occurring within a temperature range of 250–380 °C, had the fastest rate of SMPF mass loss at 350 °C. This was due to the breakage of the ether bridge bond ( $\text{Ar}-\text{CH}_2-\text{O}-\text{CH}_2-\text{Ar}$ ) in the phenolic structure into the more stable methylene-bridge bond ( $\text{Ar}-\text{CH}_2-\text{Ar}$ ), leading to a 40 % weight reduction in SMPF, the highest of the three stages. In the final stage, the rate of SMPF mass loss gradually decreased and eventually stopped. A comparison of the TGA curves of SMPF under air and nitrogen revealed that SMPF possessed a higher service temperature under nitrogen.

The thermal stability properties under nitrogen of SMPFCs are shown in Fig. 4. An increase in inorganic nano-fillers led to a gradual improvement in the thermal stability performance of SMPFCs. As illustrated in Fig. 4(a), the initial disintegration temperature of SMPFCs increased with increasing in  $\text{SiO}_2$  content, and was significantly higher than that of SMPFs. The residual carbon rate of each SMPF/ $\text{SiO}_2$  sample was higher than that of SMPF. The SMPF/ $\text{SiO}_2$ -4 sample had the highest

residual carbon rate, which gradually increased with the increasing  $\text{SiO}_2$  mass fraction in the composite foams. A similar trend was observed in SMPF/ $\text{Al}_2\text{O}_3$ . The incorporation of  $\text{Al}_2\text{O}_3$  particles improved the mass fraction of foam remaining at 1000 °C. This phenomenon is attributed to the good thermal stability of the inorganic nanoparticles, when the temperature was increased to 1000 °C, the polymer matrix in the SMPFCs was pyrolyzed, however the inorganic nanoparticles were not pyrolyzed, thus improving the residual carbon rate and thermal stability of the SMPFCs. However, the effect on the residual mass fraction of SMPF decreased with increasing content. This is attributable to the compatibility of inorganic particles in organic polymers.

### 3.3. Dynamic mechanical properties of shape memory phenolic resin and shape memory phenolic resin composites

In this study, DMA tests were utilized to observe the fluctuation in the energy storage modulus and the loss factor (Tan Delta) as a function of temperature. The storage modulus signifies the capability of materials to deform. Materials exhibiting a low storage modulus are susceptible to deformation. Tan Delta reflects the internal energy dissipation within the polymer. Polymers with a narrow Tan Delta peak can rapidly respond to changes in the external environment [34]. The Tg of SMPRs and SMPFCs were determined by DMA tests, and the shape transition temperature of each SMPF and SMPFC was subsequently identified. As illustrated in Fig. 5(a), the Tg of SMPR-1, SMPR-2, SMPR-3, and SMPR-4 were 92 °C, 86 °C, 80 °C, and 78 °C, respectively. When the temperature was above the Tg, there was an increased molecular chain segment activity, facilitating molecular motion. The data presented in Fig. 5(b) revealed that the storage modulus of SMPR decreased in conjunction with an increase in HDI content, while the Tg also decreased. Moreover, the loss modulus of SMPR-4 was lower than that of the other samples at any given temperature, suggesting that samples with a high HDI dosage had a comparably low crosslink density and spatial molecular network.

Following the incorporation of inorganic particles, the dynamic mechanical properties of the composites were measured and are shown in Fig. 5(c–f). The Tg of SMPR/ $\text{SiO}_2$  was 89.5 °C, which is notably higher

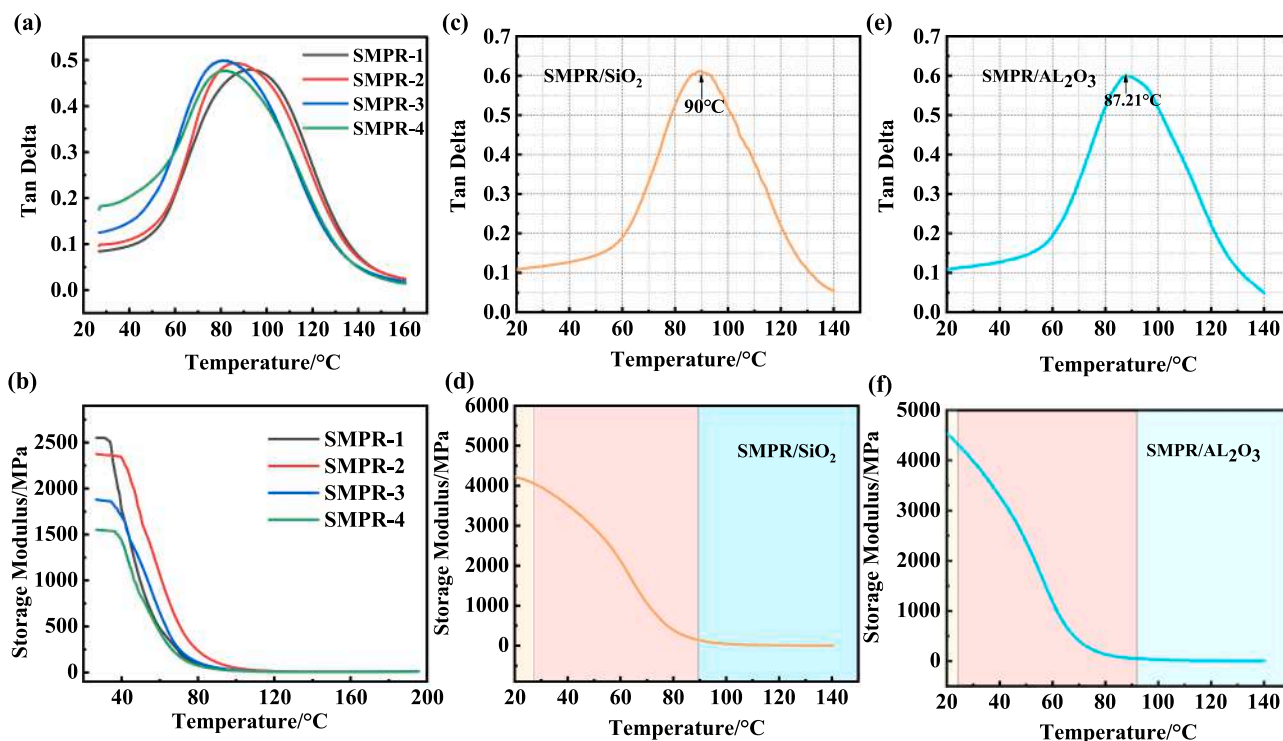


Fig. 5. (a) and (b) DMA curve of SMPRs; (c) and (d) DMA curve of SMPF/ $\text{SiO}_2$ s; (e) and (f) DMA curve of SMPF/ $\text{Al}_2\text{O}_3$ s.

than that of SMPR-4 (78 °C). At lower temperatures, the energy storage modulus of SMPR/SiO<sub>2</sub> was approximately 4.1 GPa, surpassing the 1.6 GPa storage modulus of SMPR-4, which contains an equivalent proportion of flexible chain segments. Consequently, the resistance to deformation of SMPR/SiO<sub>2</sub> improved with the addition of SiO<sub>2</sub>. As demonstrated in Fig. 5(e), the T<sub>g</sub> of SMPR/Al<sub>2</sub>O<sub>3</sub> was 87.21 °C, which also exceeded that of SMPR-4 (78 °C). At lower temperatures, the energy storage modulus of SMPR/Al<sub>2</sub>O<sub>3</sub> was approximately 4.5 GPa. The emergence of Tan Delta peaks in the composites signified that reversible states were still present in the molecular network. Additionally, the integration of inorganic particles partially restricted the movement of chain segments, leading to a minor increase in the T<sub>g</sub> of the SMPR.

### 3.4. Mechanical properties of shape memory phenolic foam and shape memory phenolic foam composites

Unlike typical foams, SMPF exhibits variable mechanical properties at different temperatures. Compression testing of SMPFs at room temperature can provide insights into the dimensional stability and compression resistance of the foam. SMPFs exhibit brittleness and possess good dimensional stability at this temperature. When compressed at room temperature, an SMPF can only undergo slight deformation before sustaining damage due to an increased load. The maximum compressive strain of materials represents the most strain value a brittle material can withstand before it fails under compression. For SMPFs, the maximum compressive strain is related to the toughness of the material. As demonstrated in Fig. 6(a), SMPFs can only be compressed to less than 5 % compressive strain at room temperature. The maximum compressive strain of SMPF-1 was the smallest at 1.2 %; the maximum compressive strain of SMPF-2 was marginally higher than that of SMPF-1, at 2.5 %; the maximum compressive strain of SMPF-3 was 3.1 %; and the maximum compressive strain of SMPF-4 was 4.6 %, indicating that SMPF-4 had the highest toughness. This characteristic is related to the ratio of flexible chain segments in SMPF. As SMPF-4 contained the highest proportion of flexible chain segments, it exhibited the highest toughness and the largest maximum compressive strain. In this group of foams, the compressive strength of the material ranges from a minimum of 72 KPa for SMPF-1 to a maximum of 98 KPa for

SMPF-2, with minor differences between individual samples. The introduction of an appropriate amount of flexible chain segments can enhance the closed porosity of the phenolic foam, thus improving the load-bearing capacity of the foam. However, the introduction of an excessive amount of long flexible chains can lead to a decrease in the cross-link density of the phenolic resin, resulting in a reduction in the compression strength of the foam.

To explore the compression behaviour of SMPFs at temperatures exceeding the T<sub>g</sub>, the foam was tested in compression at 120 °C. The experimental methodology involved increasing the temperature to 120 °C and sustaining it for 15 min to ensure the SMPFs were completely softened. Subsequently, the SMPFs were compressed to a deformation of 30 % at a rate of 0.8 mm/min. The compressive stress–strain curves of the SMPFs at 120 °C are displayed in Fig. 6(b). Here, SMPF-1, SMPF-2, SMPF-3, and SMPF-4 exhibited a stress of 33.5, 29.5, 28.8, and 22 KPa, respectively, at a 30 % strain. This phenomenon relates to the T<sub>g</sub> of the SMPFs, which decreases as the proportion of HDI involved in the reaction increases. Thus, with the temperature increase to 120 °C, SMPF-1 was the most rigid, while SMPF-4 was the softest. Furthermore, the curves suggest that the compression of SMPFs at 120 °C did not significantly change from the elastic phase to the yield phase. As the strain transitioned from 0 to 30 %, the compression of the SMPFs occurred over two stages. Under the application of unidirectional compression, the deformation was linearly elastic when the strain of the SMPF was less than 11 %. At this stage, the load was primarily supported by the bubble pores in the SMPF, and the stress and strain maintained a roughly proportional relationship. As the load continued to increase, the strain increased, marking the commencement of the second stage where the strain shifted from 10 to 30 %. During this stage, the bubble pores of the foam progressively diminished, increasing the density and triggering substantial changes in the elastic modulus of the foam.

As illustrated in Fig. 6(c), the maximum compressive stress of SMPFC increased from SMPF/SiO<sub>2</sub>-1 to SMPF/SiO<sub>2</sub>-4, and the maximum compressive strain progressively decreased as the mass fraction of the doped SiO<sub>2</sub> increased. The maximum compressive stress of the four samples did not vary significantly before the onset of damage, and all displayed a considerable increase compared to SMPFs. This increase was attributed to the integration of inorganic particles, which reduced the

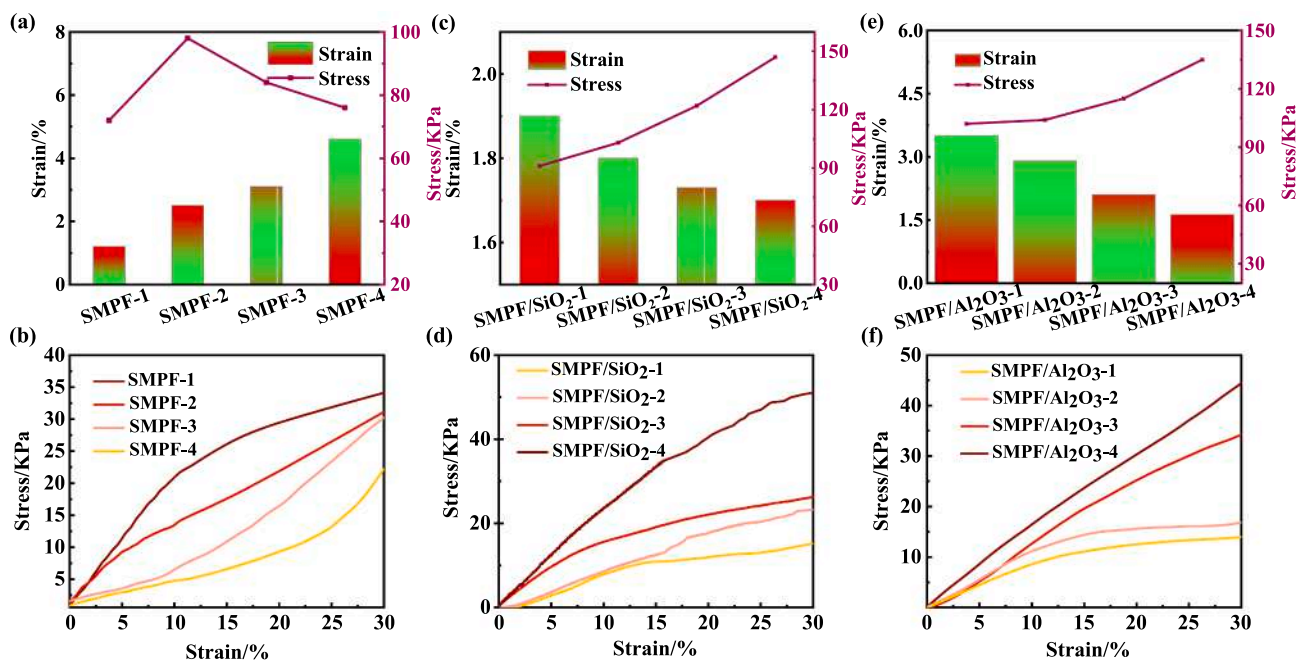


Fig. 6. The compressive stress and strain of (a) SMPFs, (c) SMPF/SiO<sub>2</sub>s, and (e) SMPF/Al<sub>2</sub>O<sub>3</sub>s in room temperature; the compressive stress–strain curve of (b) SMPFs, (d) SMPF/SiO<sub>2</sub>s, and (f) SMPF/Al<sub>2</sub>O<sub>3</sub>s at 120 °C.

pore size of the SMPFs while the uniformity of the pores increased. Classical nucleation theory proposes that inorganic nanoparticles can function as nucleating agents, affecting the foaming process of polymers. The presence of insoluble solid particles in the system decreases the amount of free energy required for heterogeneous nucleation compared to that required for homogeneous nucleation, making it easier for the latter to occur. Consequently, an appropriate number of inorganic nanoparticles can stimulate bubble nucleation, leading to more homogeneous pores in the foam. Foam composites with a more evenly distributed pore structure can withstand higher compressive stresses. Therefore, all SMPFCs exhibit elevated maximum compressive stresses relative to SMPF. The strengthening effect of SMPF/SiO<sub>2</sub>-4 was the most evident, with the compression strength at the time of damage being 148 KPa, approximately 50 % higher than that before strengthening. As demonstrated in Fig. 6(e), when the proportion of Al<sub>2</sub>O<sub>3</sub> increased, the maximum compressive strain of the composite foam gradually decreased, while the maximum compressive stress increased incrementally. The largest maximum compressive strain was observed in SMPF/Al<sub>2</sub>O<sub>3</sub>-1, measuring 3.76 %. Compared to SMPFs, the compressive strength of the SMPFCs was increased. The largest compressive strength within this group of composite foams was noted in SMPF/Al<sub>2</sub>O<sub>3</sub>-4, which reached 135 KPa, augmenting the compressive strength of SMPF by 35 %.

In assessing the compression performance of the SMPFCs at temperatures surpassing T<sub>g</sub>, compression tests were conducted on the

SMPFC at 120 °C. The foam samples were shaped as small cylinders, each with a diameter and height of 10 mm. As shown in Fig. 6(d), the compression curve of composite foams was split into two stages. The initial stage was the elastic compression stage, wherein the stress bore a proportional relationship to the strain. The following stage was the yielding stage, which was characterized by a decrease in the rate of stress increase with increasing strain. As the SiO<sub>2</sub> mass fraction within the foam increased, the requisite stress progressively increased. The stress of SMPR/SiO<sub>2</sub>-4, containing the highest SiO<sub>2</sub> mass fraction, compressed to 30 % strain, equalled 47 KPa. This value is significantly higher than that of SMPF-4 at 120 °C, suggesting that the reinforcing effect of SiO<sub>2</sub> on SMPF remained operative even when the foam inhabited a highly elastic state. As SMPFC was compressed at elevated temperatures, the soft polymer matrix could be compressed and transformed. Conversely, the inorganic nanoparticles did not undergo deformation or concurrent movement easily, thereby obstructing the deformation of the SMPFCs. Consequently, when the strain reached 30 %, the required stress for SMPFCs surpassed that for the SMPFs. This circumstance was also observable in SMPF/Al<sub>2</sub>O<sub>3</sub>. At 120 °C, the elastic modulus of the composite foam was substantially inferior compared to its state at room temperature. The composite foam demonstrated enhanced deformation capability at this stage, and could be readily compressed to 30 % strain without compromising the structural integrity of the foam. However, the inorganic nanoparticles were difficult to be distributed in the polymer matrix uniformly when the addition

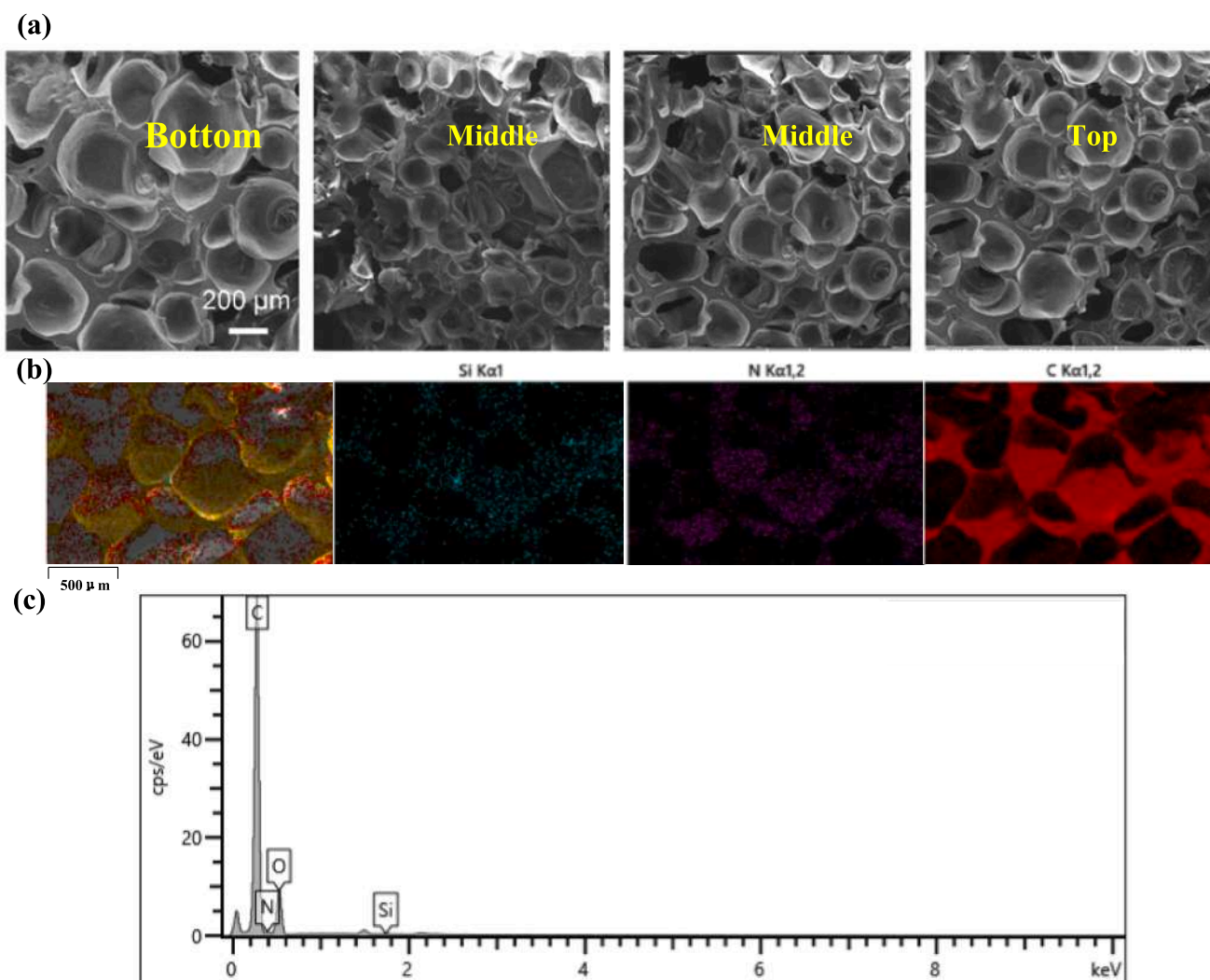


Fig. 7. (a) Morphology of SMPF at different positions; (b) elemental mapping and (c) EDS survey spectrum of SMPF/SiO<sub>2</sub>.

amount is small, the enhancement effect on the foam in the soft state was only achieved when the addition of SiO<sub>2</sub> or Al<sub>2</sub>O<sub>3</sub> was higher than 8 wt %.

### 3.5. Microstructural characterization of shape memory phenolic foam and shape memory phenolic foam composites

The microstructure of the SMPF was studied via scanning electron microscopy, as shown in Fig. 7(a). There were small perforations located on the localized bubble pores at the bottom of the foam. The size of the bubble pores in this area is larger than other parts. The bubble pores in the middle of the foam were smaller and exhibited a more consistent distribution than those at the bottom, which was attributed to the compression of the foam by the surrounding bubble pores during the foaming process. The bubble pores at the top of the foam were the most evenly distributed throughout the foam. Observations indicated that the bubble diameter of the foam produced under such foaming conditions was approximately 350–450 μm at the bottom, 150–250 μm in the middle, and 200–400 μm at the top.

The energy dispersive spectrometer (EDS) was utilized to observe the element distribution in composite foams, confirming the homogeneous dispersion of inorganic nanoparticles in the foams. As demonstrated in Fig. 7(b) and (c), the silicon element was uniformly distributed on the walls of the bubble pores of the SMPF/SiO<sub>2</sub>, and the incorporation of silica nanoparticles did not disrupt the bubble structure of the foam.

### 3.6. Shape memory performance of shape memory phenolic foam and shape memory phenolic foam composites

The shape memory cycling curve of SMPF was obtained through DMA compression thermal cycling of the foam, a process that enables the characterization and verification of the shape memory properties of SMPF. As Fig. 8(a) illustrates, SMPF exhibited excellent shape memory performance across three distinct shape memory cycles. The shape fixation rates of SMPF for these cycles were 98.7 %, 98.4 %, and 98 %, whereas the shape reversion rates for the same cycles were 82.3 %, 76.4 %, and 61.8 % respectively. During compression thermal cycling, the maximum compression strain of SMPF remained relatively consistent, though the recovery and fixation rates of SMPF gradually decreased as the number of cycles increased. The shape memory recovery and fixation rates, determined from the foam shape memory cycling experiments conducted in the laboratory, are shown in Fig. 8(b). Owing to the shape recovery process specific to the SMPF specimens, the shape recovery and fixation rates were computed for all four samples. As indicated in the figure, after the completion of five shape memory cycles, all SMPFs maintained a high shape fixation rate, despite the notable decline in the shape recovery rate. Of the four specimens, SMPF-1 exhibited the lowest

shape fixation rate and the lowest shape recovery rate, which was only 60 % after five cycles. This phenomenon was directly linked to the low crosslink density of SMPF-1. As the number of compression cycles increased, the shape fixation rate (along with shape recovery rate of all four samples) significantly decreased. This reduction was attributable to the crystallisation of the SMPs network structure. It is likely that following numerous additional shape memory compression cycles, the soft segments within the SMPFs would crystallised less easily. Consequently, the recovery force of SMPFs for shape memory recovery would consistently decrease, eventually becoming insufficient to support a return to the initial height. These results were consistent with the mechanical thermal cycling outcomes of the foam, thereby again demonstrating the excellent shape memory performance of SMPF.

The shape memory cycle of the SMP can be summarised as a situation wherein the sample is subjected to a temporary shape by external loading when it is heated above T<sub>g</sub>. Subsequently, the sample in this temporary shape becomes “frozen” by removing the external force after it cools below T<sub>g</sub>. Upon reheating the sample above T<sub>g</sub>, the temporary shape can be “unfrozen” and recovered to its initial shape. The shape memory cycle of the cylindrical foam is depicted in Fig. 9(a). To evaluate the shape memory properties of SMPF, a cylinder of SMPF with a diameter of 20 mm and a length of 30 mm was fabricated. The initial height of SMPF was 30 mm. It was heated above T<sub>g</sub> and then compressed to a height of 15 mm. Following this, the shape was fixed by cooling. The shape recovery process was subsequently monitored on a heating table at 130 °C. It was observed that the foam almost failed to recover during the initial 20 s, owing to a substantial loss of heat in the open environment. However, post-20 s, the foam began to recover, the recovery rate accelerated, and ultimately, the shape reversion was completed within 60 s (Fig. 9(b)). The shape recovery rate of the SMPF was found to be significantly influenced by the environment. As a consequence of its structural characteristics, multiple internal heat transfer modes existed within the foam material: thermal convection formed by the solid phase and gas, coupled heat transfer via the gas phase, and thermal radiation generated by the solid surface. At temperatures below 60 °C, the shape recovery rate of the foam was 0 %, ensuring complete fixation. As the ambient temperature neared the T<sub>g</sub> of the SMPF, it became easier for the SMPF to return to its original shape.

In addition to the cylindrical foam, SMPFC can also be prepared in various other shapes to complete the shape recovery process following multi-dimensional deformation. As illustrated in Fig. 9(c) and (d), the M-type SMPFC can spontaneously fold and expand when subjected to heat. Notably, the M-type SMPFC can still be compressed and deformed in the thickness direction during deformation.

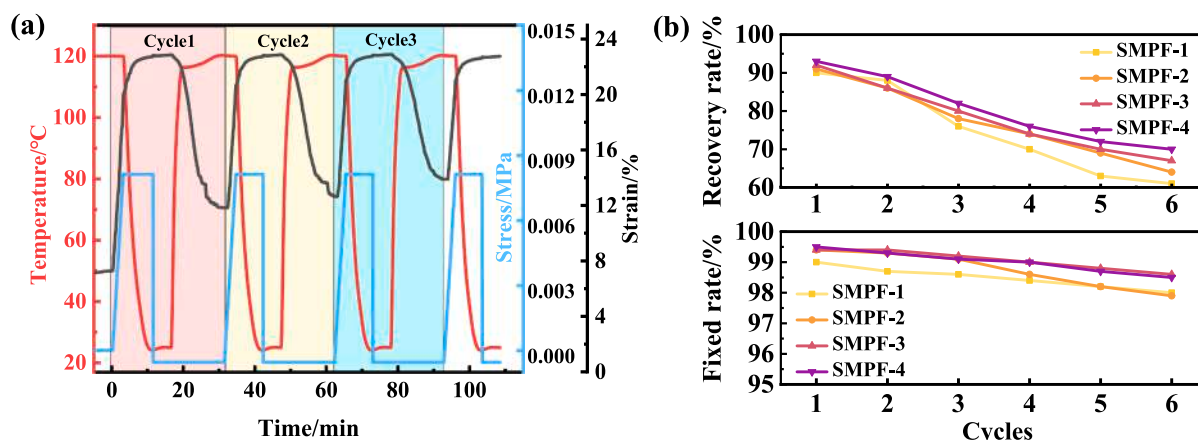


Fig. 8. (a) Shape memory cycle of SMPF; (b) the shape fixity rate and shape recovery rate of SMPFs.

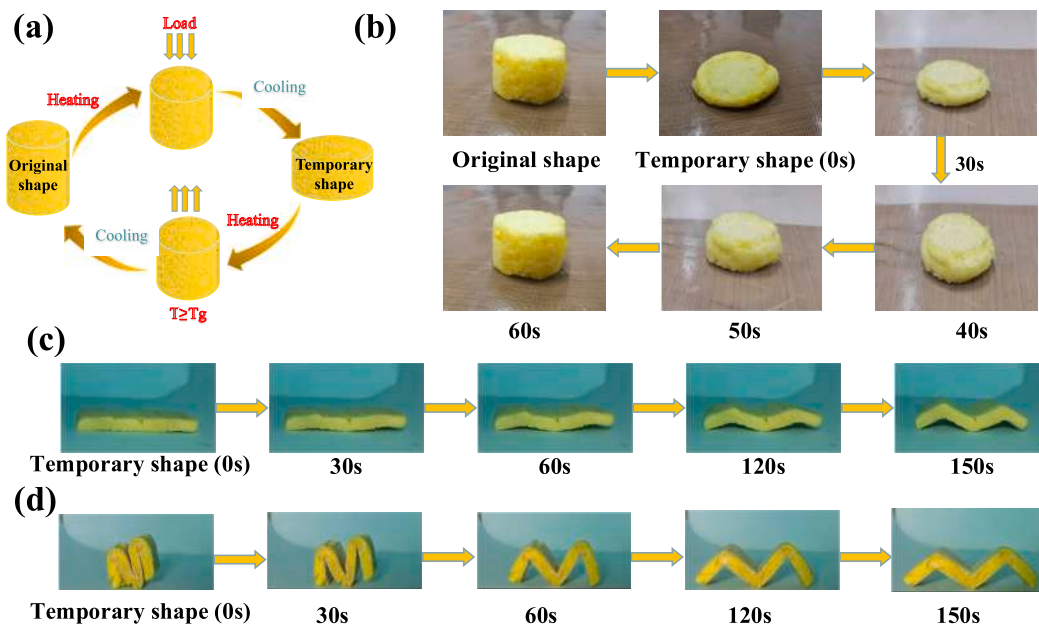


Fig. 9. (a) Schematic diagram of the shape memory process; (b) shape memory performance of cylindrical SMPF; shape memory performance of M-type SMPFC: (c) self-folding process and (d) self-expanding process.

#### 4. Conclusions

In this study, a series of SMPFs and SMPFCs with good shape memory properties, high thermal stability, and excellent mechanical properties were prepared. They were developed from SMPR and foamed via a physical method. Notably, the SMPFs exhibit good thermal stability under the test conditions, and similarly, the SMPFCs exhibit superior thermal stability similarly. The prepared foams possess a decent comprehensive property of thermal stability, mechanical properties, and deformability. SMPFs exhibit excellent shape memory performance, with the shape fixation rate maintained at approximately 98 % and the SMPF had completely expanded within 120 s via heat conduction. Excellent shape memory properties mean that the foam shows considerable promise for engineering applications such as foam plugging agents. Considering the excellent deformability and good thermal stability properties of SMPF, it also presents potential applications in aerospace flexible devices and smart fireproof materials, such as smart firewalls, smart fire blankets.

#### CRediT authorship contribution statement

**Likai Hu:** Methodology, Writing – original draft. **Fenghua Zhang:** Writing – review & editing, Project administration. **Lan Luo:** Data curation. **Linlin Wang:** Investigation. **Yanju Liu:** Resources, Supervision. **Jinsong Leng:** Resources, Supervision, Funding acquisition.

#### Declaration of Competing Interest

The authors declare that they have no known competing financial interests or personal relationships that could have appeared to influence the work reported in this paper.

#### Data availability

Data will be made available on request.

#### Acknowledgements

This work was financially supported by the National Key R&D Program of China (2022YFB3805700) and National Natural Science

Foundation of China (Grant No. 92271112).

#### References

- [1] Leng J, Lan X, Liu Y, Du S. Shape-memory polymers and their composites: stimulus methods and applications. *Prog Mater Sci* 2011;56(7):1077–135.
- [2] Xu T, Li G. A shape memory polymer based syntactic foam with negative Poisson's ratio. *Mater Sci Eng A-Struct Mater Propert Microstruct Process* 2011;528(22–23):6804–11.
- [3] Lendlein A, Jiang H, Junger O, Langer R. Light-induced shape-memory polymers. *Nature* 2005;434(7035):879–82.
- [4] Zhao F, Zheng X, Zhou S, Zhou B, Xue S, Zhang Y. Constitutive model for epoxy shape memory polymer with regulable phase transition temperature. *Int J Smart Nano Mater* 2021;12(1):72–87.
- [5] Luo L, Zhang F, Pan W, Yao Y, Liu Y, Leng J. Shape memory polymer foam: active deformation, simulation and validation of space environment. *Smart Mater Struct* 2022;31(3):035008.
- [6] Li G, Uppu N. Shape memory polymer based self-healing syntactic foam: 3-D confined thermomechanical characterization. *Compos Sci Technol* 2010;70(9):1419–27.
- [7] Metcalfe A, Desfaits A-C, Salazkin I, Yahia LH, Sokolowski WM, Raymond J. Cold hibernated elastic memory foams for endovascular interventions. *Biomaterials* 2003;24(3):491–7.
- [8] Zhu S, Zhou Q, Wang M, Dale J, Qiang Z, Fan Y, et al. Modulating electromagnetic interference shielding performance of ultra-lightweight composite foams through shape memory function. *Compos Part B-Eng* 2021;204:108497.
- [9] Chung SE, Park CH. The thermoresponsive shape memory characteristics of polyurethane foam. *J Appl Polym Sci* 2010;117(4):2265–71.
- [10] Curtis SM, Sielenkämper M, Arivanandhan G, Dengiz D, Li Z, Jetter J, et al. TiNiHf/SiO<sub>2</sub>/Si shape memory film composites for bi-directional micro actuation. *Int J Smart Nano Mater* 2022;13(2):293–314.
- [11] Singhal P, Rodriguez JN, Small W, Eagleston S, Van de Water J, Maitland DJ, et al. Ultra low density and highly crosslinked biocompatible shape memory polyurethane foams. *J Polym Sci B: Polym Phys* 2012;50(10):724–37.
- [12] Jang LK, Nash LD, Fletcher GK, Cheung T, Soewito A, Maitland DJ. Enhanced X-ray visibility of shape memory polymer foam using iodine motifs and tantalum microparticles. *J Compos Sci* 2021;5(1):14.
- [13] King O, Constant E, Weems AC. Shape memory poly(beta-hydroxythioether) foams for oil remediation in aquatic environments. *ACS Appl Mater Interfaces* 2021;13(17):20641–52.
- [14] Sauter T, Kratz K, Madbouly S, Klein F, Heuchel M, Lendlein A. Anisotropy effects in the shape-memory performance of polymer foams. *Macromol Mater Eng* 2021;306(4):2170015.
- [15] Jia X, Shen B, Zhang L, Zheng W. Construction of shape-memory carbon foam composites for adjustable EMI shielding under self-fixable mechanical deformation. *Chem Eng J* 2021;405:126927.
- [16] Santo L, Bellisario D, Iorio L, Quadrini F. Shape memory composite structures for self-deployable solar sails. *Astrodynamics* 2019;3(3):247–55.
- [17] Santo L, Quadrini F, Mascetti G, Dolce F, Zolesi V. Mission STS-134: results of shape memory foam experiment. *Acta Astronaut* 2013;91:333–40.

- [18] Lan X, Liu L, Zhang F, Liu Z, Wang L, Li Q, et al. World's first spaceflight on-orbit demonstration of a flexible solar array system based on shape memory polymer composites. *Sci China-Technol Sci* 2020;63(8):1436–51.
- [19] Quadri F, Santo L, Squeo EA. Solid-state foaming of nano-clay-filled thermoset foams with shape memory properties. *Polym-Plast Technol Eng* 2012;51(6):560–7.
- [20] Li G, King A, Xu T, Huang X. Behavior of thermoset shape memory polymer-based syntactic foam sealant trained by hybrid two-stage programming. *J Mater Civ Eng* 2013;25(3):393–402.
- [21] Zhang F, Zhou T, Liu Y, Leng J. Microwave synthesis and actuation of shape memory polycaprolactone foams with high speed. *Sci Rep* 2015;5.
- [22] Tondi G, Zhao W, Pizzi A, Du G, Fierro V, Celzard A. Tannin-based rigid foams: a survey of chemical and physical properties. *Bioresour Technol* 2009;100(21):5162–9.
- [23] Yu Z-L, Li G-C, Fechner N, Yang N, Ma Z-Y, Wang X, et al. Polymerization under hypersaline conditions: a robust route to phenolic polymer-derived carbon aerogels. *Angew Chem-Int Ed* 2016;55(47):14623–7.
- [24] Lou Z, Li Ru, Wang P, Zhang Y, Chen Bo, Huang C, et al. Phenolic foam-derived magnetic carbon foams (MCFs) with tunable electromagnetic wave absorption behavior. *Chem Eng J* 2020;391:123571.
- [25] Sarika PR, Nancarrow P, Khansaheb A, Ibrahim T. Bio-based alternatives to phenol and formaldehyde for the production of resins. *Polymers* 2020;12(10):2237.
- [26] Li B, Wang Y, Mahmood N, Yuan Z, Schmidt J, Xu C. Preparation of bio-based phenol formaldehyde foams using depolymerized hydrolysis lignin. *Ind Crop Prod* 2017;97:409–16.
- [27] Li B, Yuan Z, Schmidt J, Xu C. New foaming formulations for production of bio-phenol formaldehyde foams using raw kraft lignin. *Eur Polym J* 2019;111:1–10.
- [28] Yu K, Luo X, Wang M, Qian K. Preparation and characterization of phenolic foam reinforced with expandable graphite and expanded graphite. *J Cell Plast* 2018;54(3):545–59.
- [29] Sui X, Wang Z. Flame-retardant and mechanical properties of phenolic foams toughened with polyethylene glycol phosphates. *Polym Adv Technol* 2013;24(6):593–9.
- [30] Luo X, Yu K, Qian K. Morphologies and compression performance of graphene oxide/SiO<sub>2</sub> modified phenolic foam. *High Perform Polym* 2018;30(7):803–11.
- [31] Deng Y, Zhang F, Liu Y, Leng J. Design and synthesis of shape memory phenol-formaldehyde with good irradiation resistance, thermal, and mechanical properties. *ACS Appl Polym Mater* 2022;4(8):5789–99.
- [32] Walter M, Friess F, Krus M, Zolanvari SMH, Grün G, Kröber H, et al. Shape memory polymer foam with programmable apertures. *Polymers* 2020;12(9):1914.
- [33] Li F, Liu L, Lan X, Pan C, Liu Y, Leng J, et al. Ground and geostationary orbital qualification of a sunlight-stimulated substrate based on shape memory polymer composite. *Smart Mater Struct* 2019;28(7):075023.
- [34] Nejad HB, Baker RM, Mather PT. Preparation and characterization of triple shape memory composite foams. *Soft Matter* 2014;10(40):8066–74.